Supplemental Document

OPTICA

Optically derived radio-frequency benchmark in methanol: a sub-kHz reference for astrophysical tests of fundamental physics: supplement

Frank M. J. Cozijn,[1,2] Arthémise Altman,[1] Alexandr S. Bogomolov,[1] Alexis Libert,[1] Simon Collignon,[1] Erik Dierikx,[3] Jeroen C. J. Koelemeij,[2] Boy Lankhaar,[4] Isabelle Kleiner,[5] Clément Lauzin,[1] and Wim Ubachs[2,]

[1] *Institute of Condensed Matter and Nanosciences, Université catholique de Louvain, Louvain-la-Neuve, Belgium*
[2] *Department of Physics and Astronomy, LaserLab, Vrije Universiteit De Boelelaan 1100, Amsterdam 1081 HZ, The Netherlands*
[3] *VSL Dutch Metrology Institute, Thijsseweg 11, Delft 2629 JA, The Netherlands*
[4] *Institute of Theoretical Astrophysics, The Faculty of Mathematics and Natural Sciences, University of Oslo, Sem Sælands vei 13, Oslo, Norway*
[5] *Université Paris Cité and Univ Paris Est Creteil, CNRS, LISA, Paris F-75013, France*

Supplement DOI: https://doi.org/10.6084/m9.figshare.32659998

Parent Article DOI: https://doi.org/10.1364/OPTICA.593388

Supplementary Material

Optically Derived Radio-Frequency Benchmark in Methanol: A Sub-kHz Reference for Astrophysical Tests of Fundamental Physics

Frank M. J. Cozijn,[1,2] Arthémise Altman,[1] Alexandr S. Bogomolov,[1] Alexis Libert,[1] Simon Collignon,[1] Erik Dierikx,[3] Jeroen C. J. Koelemeij,[2] Boy Lankhaar,[4] Isabelle Kleiner,[5] Clément Lauzin,[1] and Wim Ubachs[2]

[1]*Institute of Condensed Matter and Nanosciences, Université catholique de Louvain, Louvain-la-Neuve, Belgium*

[2]*Department of Physics and Astronomy, LaserLab, Vrije Universiteit De Boelelaan 1100, 1081 HZ Amsterdam, The Netherlands*

[3]*VSL Dutch Metrology Institute, Thijsseweg 11, 2629 JA Delft, The Netherlands*

[4]*Institute of Theoretical Astrophysics, The Faculty of Mathematics and Natural Sciences, University of Oslo, Sem Sælands vei 13, Oslo, Norway*

[5]*Université Paris Cité and Univ Paris Est Creteil, CNRS, LISA, F-75013 Paris, France*

I. QUANTITATIVE LINESHAPE EFFECTS OF THE HYPERFINE STRUCTURE IN THE 3_{-1}E - 2_0E TRANSITION WITHIN THE GROUND VIBRATIONAL STATE

In the main text, the centroid shift of the $2_0E \leftarrow 3_{-1}E$ rotational transition within the ground vibrational manifold of methanol (CH_3OH) is discussed. Because the specific hyperfine coupling constants for the highly excited rovibrational states near 1.4 μm are currently unavailable, this section provides a detailed numerical demonstration of lineshape distortions and line pulling effects utilizing the known ground-state hyperfine structure. This analysis serves as a representative verification model under the assumption that the hyperfine splittings in the vibrationally excited states are highly similar in character and magnitude to those of the ground state.

We perform a comprehensive numerical simulation to evaluate the coupled effects of the unresolved hyperfine structure and the large-amplitude wavelength modulation (dither) on the observed lineshape. The 22 underlying hyperfine transitions and their associated frequency shifts (ΔE) as documented by Lankhaar et al. [1] are consolidated in Table I, along with the Einstein A-coefficients used in the analysis.

For each hyperfine component the Einstein A-coefficients are taken as proportional to the $S\mu^2$ intensities included in the computation of the centroid frequency shift. Since the NICE-OHMS technique registers the dispersive phase response of a molecular transition, each hyperfine sub-component is initially modeled as an individual, unmodulated direct dispersive Lorentzian profile of the form:

$$S_{\mathrm{disp},i}(\nu) = A_i \frac{\nu - \nu_i}{\Gamma^2 + 4(\nu - \nu_i)^2}, \tag{1}$$

where ν_i is the frequency position of the i-th hyperfine component, A_i is its respective amplitude proportional to the line strength, and Γ is the unmodulated full-width at half-maximum (FWHM) homogeneous linewidth parameter. The composite unmodulated dispersion spectrum is constructed via a direct linear summation of these individual profiles, expressed as $S_{\mathrm{comp}}(\nu) = \sum_i S_{\mathrm{disp},i}(\nu)$.

TABLE I. Transitions between hyperfine levels with quantum numbers F_{J,K_a} within the rotational transition 2_0E and $3_{-1}E$ at 12.178 GHz.

F_{2_0}	$F_{3_{-1}}$	ΔE (kHz)	A ($10^{-9}\,\mathrm{s}^{-1}$)
3	4	4.965	7.372
3	3	3.306	0.293
3	3	-9.120	0.344
3	2	-14.335	0.018
2	3	4.802	7.519
2	3	-7.624	0.221
2	2	-12.839	0.287
2	3	7.667	0.098
2	3	-4.760	7.325
2	2	-9.974	0.605
1	2	-7.978	8.027
2	3	1.475	5.711
2	3	-11.352	1.495
2	2	-17.669	0.821
3	4	6.106	7.372
3	3	5.844	0.325
3	3	-6.982	0.312
3	2	-13.300	0.018
2	3	6.980	1.861
2	3	-5.847	6.095
2	2	-12.164	0.071
1	2	-3.263	8.027

To isolate any systematic line-pulling contributions driven purely by the intrinsic asymmetry of the intensity distribution, this composite unmodulated dispersion spectrum is fitted with a single analytical dispersive Lorentzian function. From this fit, we extract a negligible additional lineshape broadening of only ~ 1 kHz relative to the parent molecular linewidth, alongside an entirely minor center frequency pulling offset of $\nu_{\text{fit}} - \nu_{\text{c}} \approx 3$ Hz for an input width of $\Gamma_{\text{true}} = 300$ kHz.

To evaluate the profile behavior under standard experimental conditions, two separate, parallel $1f$ lineshape tracking scenarios are calculated. First, to accurately simulate our experimental wavelength modulation spectroscopy (WMS) implementation, a sinusoidal frequency modulation with a peak-to-peak dither amplitude of 150 kHz is numerically applied to the composite dispersion profile over a complete modulation cycle, and the first harmonic (1f) is extracted via numerical integration. This modulation introduces an additional broadening of approximately 38 kHz to the fitted profile ($\Gamma \approx 339$ kHz), which closely mimics the modulation-induced broadening observed in our measurements. Fitting this dithered profile results in a center tracking error of only $\nu_{\text{fit}} - \nu_{\text{c}} \approx 5$ Hz.

Second, we evaluate the theoretical limit of an infinitesimally small modulation amplitude by computing the pure analytical first derivative of the composite dispersion profile, $S'_{\text{comp}}(\nu) = \sum_i S'_{\text{disp},i}(\nu)$. This zero-dither configuration represents the physical "worst-case scenario" for systematic line pulling. Because there is no finite modulation dither present to smear out or average over the underlying multiplet features. Consequently, fitting this pure derivative trace yields a slightly elevated center pulling offset of $\nu_{\text{fit}} - \nu_{\text{c}} \approx 7$ Hz and reproduces the underlying width of $\Gamma \approx 301$ kHz.

Crucially, these systematic line pulling offsets are fundamentally insignificant when compared to our typical experimental uncertainties, demonstrating that hyperfine lineshape asymmetries do not limit the accuracy of our frequency extraction.

The simulated lineshapes, fits, and residuals for both modulation cases are shown in Fig. 1. The structured, symmetric residual profiles visible in the total residuals channel (Fig. 1(d)) display a high degree of qualitative agreement with the experimental spectra.

However, a key insight is revealed by inspecting the pure asymmetric residuals channel (Fig. 1(e)). The peak amplitude of the asymmetric component generated strictly by the underlying hyperfine structures is small, amounting to a relative fraction of only $\sim 4 \times 10^{-5}$ of the peak signal height. In contrast, the asymmetric residuals typically encountered in our measurements are roughly an order of magnitude larger. This experimental discrepancy shows that unmodeled molecular hyperfine structure is likely a negligible driver of experimental lineshape asymmetry.

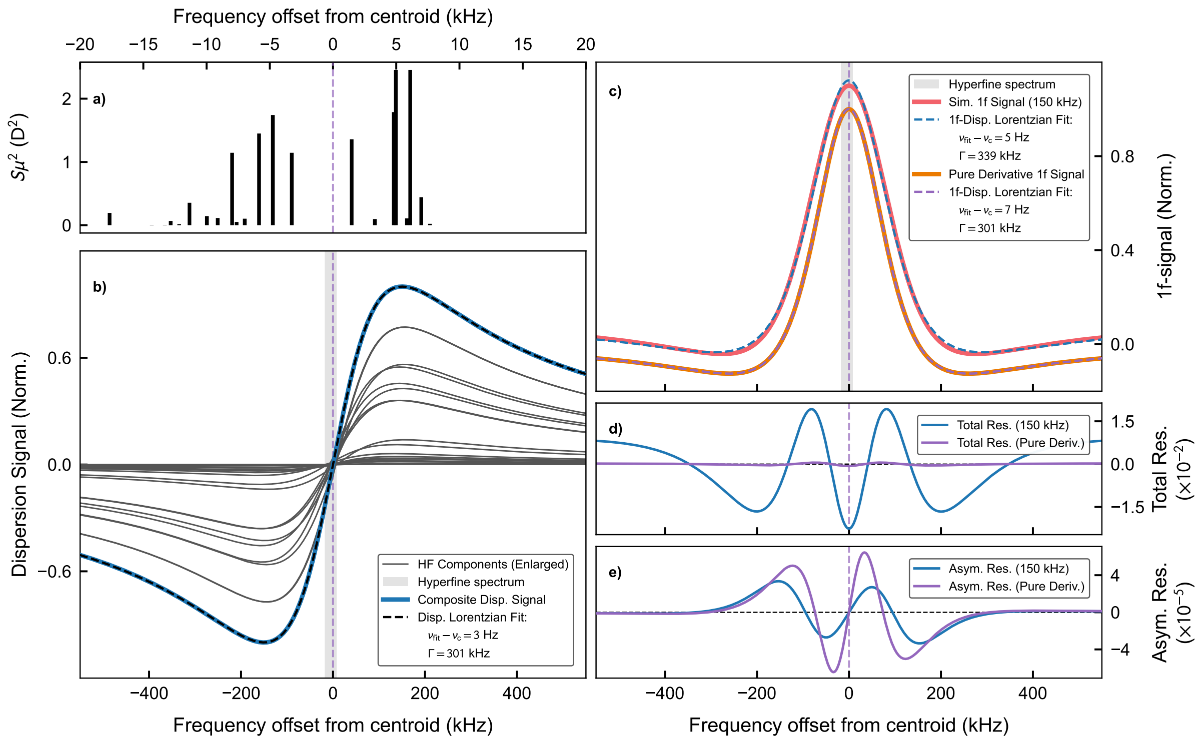

FIG. 1. Numerical lineshape simulation evaluating systematic hyperfine line pulling in the $2_0E \leftarrow 3_{-1}E$ transition of methanol ($\Gamma_{\text{true}} = 300$ kHz). (a) Relative $S\mu^2$ intensities of the 22 underlying hyperfine components. (b) Unmodulated dispersion spectrum showing individual components (gray), their convolved sum (blue), and a single-component fit (dashed black; $\nu_{\text{fit}} - \nu_c \approx 3$ Hz, $\Gamma \approx 301$ kHz). (c) Overlaid first-harmonic ($1f$) signal channels. The 150 kHz dither simulation (red) is shown with its fit (blue, vertically offset; $\nu_{\text{fit}} - \nu_c \approx 5$ Hz, $\Gamma \approx 339$ kHz). The pure derivative zero-dither limit (orange) is shown with its fit (purple; $\nu_{\text{fit}} - \nu_c \approx 7$ Hz, $\Gamma \approx 301$ kHz). (d) Total fit residuals for the 150 kHz dither (blue) and pure derivative (purple) profiles. (e) Isolated asymmetric residuals for the 150 kHz dither (blue) and pure derivative (purple) profiles. The shaded gray band marks the physical footprint of the hyperfine splitting (~ 35.3 kHz), and the vertical dashed purple line indicates the position of the central molecular centroid.

II. GENERAL FRAMEWORK ON HYPERFINE-INDUCED LINE-CENTROID SHIFTS IN ABSORPTION

The main text uses pairs of optical/infrared transitions to determine the energy separation between the $3_{-1}E$ and 2_0E levels in the vibrational ground state. For each pair, the two measured transitions share a common upper level. If the measured optical line positions are genuine differences of level energies, then the common upper level cancels from the frequency difference, and one is able to derive the radio frequency of the transition of interest from the optical measurements. The role of this section is to justify the corresponding situation when the measured line centers are shifted by unresolved hyperfine structure.

The point that requires care is the hyperfine structure of the vibration–torsion–rotation levels. In the present experiments the hyperfine components are not resolved, but they do shift the apparent line center. A priori, such a shift could be a property of the whole transition: it could depend on how the hyperfine components of one level are connected to those of the other level. If that were the case, the frequency difference of two optical lines sharing a common level would not necessarily be the difference of two transition-independent level energies, and the triangulation argument would require an additional correction.

Here we show that, under the assumptions relevant to the experiments, this complication does not arise. The centroid of an unresolved hyperfine multiplet is the difference between two level-specific hyperfine centroids. These centroids are properties of the participating vibration–torsion–rotation levels themselves and do not depend on which transition is used to probe them. To make this connection explicit, let i label one of the common upper levels in the triangulation scheme, let $j = 1, 2$ label transitions from the $3_{-1}E$ and 2_0E lower levels, respectively, and let $\nu^c_{i,j}$ denote the centroid of the corresponding unresolved optical line. We write $\bar{E}_\alpha$ for the hyperfine-corrected centroid energy of level α, with the precise definition derived below. Then, for the common upper level u_i,

$$\nu^c_{i,1} = \frac{\bar{E}_{u_i} - \bar{E}_{3_{-1}E}}{h}, \qquad \nu^c_{i,2} = \frac{\bar{E}_{u_i} - \bar{E}_{2_0E}}{h}, \tag{2}$$

so that

$$\nu^c_{i,1} - \nu^c_{i,2} = \frac{\bar{E}_{2_0E} - \bar{E}_{3_{-1}E}}{h}. \tag{3}$$

This is the hyperfine-corrected version of the triangulation scheme used in the main text. The derivation below establishes the level-centroid relation used in these equations.

We consider absorption from a lower state with good angular momentum J to an upper state with angular momentum J'. Both levels are hyperfine-split by a total nuclear spin I, forming hyperfine levels characterized by total angular momenta F and F'.

Since the relevant laboratory measurements determine line frequencies from absorption experiments, the quantity of interest is the frequency-dependent absorption coefficient, which we write as

$$\kappa_\nu = \sum_{FF'} \frac{h\nu_{FF'}}{4\pi}\, n_F\, B_{FF'}\, \phi(\nu - \nu_{FF'})\,, \tag{4}$$

where $\nu_{FF'}$ is the hyperfine transition frequency for $F \to F'$, $B_{FF'}$ is the associated Einstein B coefficient, n_F is the population of the lower hyperfine level F, and $\phi(\nu - \nu_{FF'})$ is the normalized line profile centered on $\nu_{FF'}$.

Hyperfine interactions constitute a small perturbation on the vibration–torsion–rotation structure, so the transition frequencies

$$\nu_{FF'} = \nu_0 + \Delta\nu_{FF'} \tag{5}$$

are best characterized in terms of the parent vibration–torsion–rotation frequency ν_0 and the hyperfine shift $\Delta\nu_{FF'}$. Since $\nu_0 \gg \Delta\nu_{FF'}$, it is a good approximation to set $\nu_{FF'} \approx \nu_0$ in the prefactor of κ_ν.

Furthermore, if the hyperfine sublevels are populated according to local thermodynamic equilibrium, the quantity

$$\frac{n_F}{2F+1} = N$$

is constant. Finally, the hyperfine-resolved Einstein coefficient is related to the vibration–torsion–rotation Einstein coefficient via

$$B_{FF'} = (2J+1)(2F'+1) \begin{Bmatrix} J & F & I \\ F' & J' & 1 \end{Bmatrix}^2 B_{JJ'}, \tag{6}$$

where we used the Wigner–Eckart theorem and the quantity in curly brackets is a Wigner $6j$ symbol.

Using these results, we rewrite the absorption coefficient as

$$\kappa_\nu = \frac{h\nu_0}{4\pi}\, N\,(2J+1)\, B_{JJ'} \sum_{FF'} (2F+1)(2F'+1) \begin{Bmatrix} J & F & I \\ F' & J' & 1 \end{Bmatrix}^2 \phi(\nu - \nu_{FF'})\,. \tag{7}$$

The summation is the hyperfine-resolved line profile, which we denote by Φ_ν.

For the measured transitions, line broadening renders the hyperfine structure unresolved. In that regime, hyperfine structure manifests primarily as a shift of the apparent line center, which we estimate by computing the centroid

$$\begin{aligned}\nu_c &= \frac{\int d\nu\, \nu\, \Phi_\nu}{\int d\nu\, \Phi_\nu} \\ &= \frac{\sum_{FF'}(2F+1)(2F'+1)\begin{Bmatrix} J & F & I \\ F' & J' & 1 \end{Bmatrix}^2 (\nu_0 + \Delta\nu_{FF'})}{\sum_{FF'}(2F+1)(2F'+1)\begin{Bmatrix} J & F & I \\ F' & J' & 1 \end{Bmatrix}^2}, \end{aligned} \tag{8}$$

where we used that the line profiles $\phi(\nu)$ are normalized.

We decompose the hyperfine shift into contributions from the upper and lower levels,

$$\Delta\nu_{FF'} = \delta\nu_{F'} - \delta\nu_F, \tag{9}$$

which yields

$$\begin{aligned}\nu_c = \nu_0 &+ \frac{\sum_{F'}(2F'+1)\,\delta\nu_{F'}\sum_F(2F+1)\begin{Bmatrix} J & F & I \\ F' & J' & 1 \end{Bmatrix}^2}{\sum_{FF'}(2F+1)(2F'+1)\begin{Bmatrix} J & F & I \\ F' & J' & 1 \end{Bmatrix}^2} \\ &- \frac{\sum_{F}(2F+1)\,\delta\nu_{F}\sum_{F'}(2F'+1)\begin{Bmatrix} J & F & I \\ F' & J' & 1 \end{Bmatrix}^2}{\sum_{FF'}(2F+1)(2F'+1)\begin{Bmatrix} J & F & I \\ F' & J' & 1 \end{Bmatrix}^2}. \end{aligned} \tag{10}$$

We now use the orthogonality relation

$$\sum_f (2f+1)\begin{Bmatrix} a & b & c \\ d & e & f \end{Bmatrix}^2 = \frac{1}{2c+1},$$

together with the permutation symmetries of the Wigner $6j$ symbols, to obtain

$$\sum_{F'}(2F'+1)\begin{Bmatrix} J & F & I \\ F' & J' & 1 \end{Bmatrix}^2 = \frac{1}{2J+1}, \qquad \sum_{F}(2F+1)\begin{Bmatrix} J & F & I \\ F' & J' & 1 \end{Bmatrix}^2 = \frac{1}{2J'+1},$$

and therefore

$$\sum_{FF'}(2F+1)(2F'+1)\begin{Bmatrix} J & F & I \\ F' & J' & 1 \end{Bmatrix}^2 = 2I+1.$$

With these identities, the centroid becomes

$$\nu_c = \nu_0 + \frac{1}{(2J'+1)(2I+1)}\sum_{F'}(2F'+1)\,\delta\nu_{F'} - \frac{1}{(2J+1)(2I+1)}\sum_{F}(2F+1)\,\delta\nu_F. \quad (11)$$

This is the key result that is pertinent to the triangulation scheme. For any vibration–torsion–rotation level α, the hyperfine centroid shift is

$$\bar{\delta\nu}_\alpha = \frac{1}{(2J_\alpha+1)(2I+1)}\sum_{F_\alpha}(2F_\alpha+1)\,\delta\nu_{F_\alpha}, \quad (12)$$

and the corresponding hyperfine-corrected level energy

$$\bar{E}_\alpha = E_\alpha^{(0)} + h\bar{\delta\nu}_\alpha. \quad (13)$$

The preceding expression for ν_c is then simply

$$h\nu_c = \bar{E}_f - \bar{E}_i, \quad (14)$$

where i and f denote the lower and upper vibration–torsion–rotation levels of the transition. Importantly, $\bar{E}_i$ and $\bar{E}_f$ are level properties. They do not depend on which other level is used to probe the transition. Thus the hyperfine shift of the unresolved line centroid is not an additional transition-specific correction; it is already accounted for by replacing the unperturbed level energies by their hyperfine centroids.

Finally, recalling the assumption that hyperfine splittings are much smaller than the broadening, the total profile satisfies

$$\begin{aligned}\Phi_\nu &= \sum_{FF'}(2F+1)(2F'+1)\begin{Bmatrix} J & F & I \\ F' & J' & 1 \end{Bmatrix}^2 \phi(\nu-\nu_{FF'}) \\ &\simeq \phi(\nu-\nu_c)\sum_{FF'}(2F+1)(2F'+1)\begin{Bmatrix} J & F & I \\ F' & J' & 1 \end{Bmatrix}^2 = (2I+1)\,\phi(\nu-\nu_c)\,. \quad (15)\end{aligned}$$

Together with $\nu_0 \approx \nu_c$, this leads to the absorption coefficient

$$\kappa_\nu = \frac{h\nu_c}{4\pi}\,(2J+1)(2I+1)\,N\,B_{JJ'}\,\phi(\nu-\nu_c)\,. \quad (16)$$

Therefore, in the measurements discussed in the main text, the centroid associated with each unresolved optical line is the difference of the hyperfine-corrected centroids of the two participating vibration–torsion–rotation levels. For two transitions sharing the same connecting level, that level centroid cancels in the difference, leaving the hyperfine-corrected separation of the two ground-state levels. This validates the triangulation scheme used to obtain the radio-frequency benchmark.

For methanol in particular, some hyperfine eigenstates can have mixed nuclear-spin character, i.e. they are not purely $I = 0$ or $I = 1$ but contain mixtures of both. This does not affect any of the arguments presented here.

III. ESTIMATION OF LINESHAPE ASYMMETRY UNCERTAINTY

In the main text, a lineshape asymmetry uncertainty (σ_{asym}) is assigned to account for unmodeled, non-statistical lineshape deformations that manifest as an odd-symmetric component in the fit residuals. Because the physical origin of this residual asymmetry is complex, arising from a combination of dispersion-induced cavity effects, unresolved hyperfine structure, second-order Doppler shifts, and wavelength-modulation anharmonicity, a single, deterministic analytical model of the resulting line pulling is unavailable. To establish a reliable error bound, we evaluate two alternative formulations designed to derive a conservative frequency uncertainty from the extracted residual asymmetry.

A. Error-Bounding Models

The first approach is a global linewidth-scaled envelope model. Rather than assuming the asymmetry is physically as broad as the line itself, this model conservatively treats the perturbation as if it acts across the maximum leverage arm of the transition, which corresponds to the full-width at half-maximum linewidth. By evaluating the residual amplitude over this maximum frequency scale, the model establishes a strict upper bound for a worst-case scenario. The resulting error bound ($\sigma_{\text{asym},\Gamma}$) is defined by the peak-to-peak amplitude of the isolated asymmetric residual ($S_{\text{pp,asym}}$) normalized to the peak-to-peak amplitude of the primary signal ($S_{\text{pp,signal}}$), scaled directly by the fitted full-width at half-maximum molecular linewidth (Γ):

$$\sigma_{\text{asym},\Gamma} = \Gamma \times \frac{S_{\text{pp,asym}}}{S_{\text{pp,signal}}} \tag{17}$$

The second approach is a localized, span-scaled model. Instead of scaling the uncertainty to the full linewidth of the transition, the scaling factor Γ in Eq. (17) is substituted with the localized residual span ($\delta\nu_{\text{span}}$), which varies between individual measurements. This span is defined as the frequency separation between the first local maximum and minimum of the smoothed asymmetric residual immediately adjacent to the fitted line center:

$$\sigma_{\text{asym,span}} = \delta\nu_{\text{span}} \times \frac{S_{\text{pp,asym}}}{S_{\text{pp,signal}}} \tag{18}$$

By explicitly utilizing $\delta\nu_{\text{span}}$, this second formulation accounts for localized action, testing whether a tighter metric provides a more accurate evaluation of center frequency pulling.

B. Numerical Simulation Architecture

To evaluate the performance and operational limits of both models against a known, unperturbed line center, we performed a series of numerical lineshape simulations. The complete simulation architecture and resulting trend analyses are presented in Fig. 2. Asymmetry was generated using two distinct mechanisms:

1. **Dispersive perturbation:** A pure, unperturbed theoretical $1f$-dispersive Lorentzian profile ($\Gamma_{\text{true}} = 450$ kHz) was overlaid with a dispersive Lorentzian artifact centered at zero. The injected artifact was confined by a sharp Gaussian window to reduce an unnaturally large contribution to the wings. The amplitude of the dispersive feature was iteratively scaled to force the extracted asymmetry to exactly 0.1% peak-to-peak, while the background width was swept over a wide span-to-linewidth ratio ($\delta\nu_{\text{bg}}/\Gamma_{\text{true}} = 0.1$ to 2).

2. **Hyperfine perturbation:** Rather than injecting an external background, asymmetry was generated directly from the underlying molecular structure. The full WMS composite spectrum was constructed by summing the 22 core hyperfine components of the methanol transition centered around the physical centroid. To simulate a systematic scaling distortion in the lineshape, the physical splitting constants were stretched using a multiplier swept from $1\times$ to $5\times$, generating a structurally asymmetric profile with an expanding unmodeled footprint.

In both simulation tracks, the composite perturbed profiles were processed through our standard least-squares fitting routine. The asymmetric residuals were isolated via cubic spline reflection around the fitted center (ν_{fit}) to evaluate the error bounds predicted by Eq. (17) and Eq. (18).

C. Results and Empirical Scaling

To evaluate line-pulling universally, the simulation results (Fig. 2) are plotted against the dimensionless span-to-linewidth ratio ($\delta\nu_{\text{span}}/\Gamma$). This parameter space (0 to 0.3) matches the range of residual span-to-linewidth ratios observed in our experimental data.

The numerical sweeps reveal distinct scaling behaviors. In the dispersive petrubation simulation, the global linewidth-scaled model ($\sigma_{\text{asym},\Gamma}$) predicts a flat error bound that fails to capture the true frequency shift. Conversely, the localized span-based model accurately tracks the proportional scaling of the actual center shift. An important metrological insight from this sweep is that broad residual wings outside the core linewidth do not significantly alter the line-pulling magnitude, confirming that localized asymmetry within the linewidth is the deterministic factor driving the center frequency shift.

A similar trend occurs in the hyperfine multiplet simulation, where the span-scaled bounds track the actual frequency shift much more accurately than the rigid linewidth envelope. While the unscaled $1\times$ local span formula provides a highly accurate estimate, it marginally undershoots the true physical center pulling in specific simulation extremes. To guarantee that the error budget remains rigorously bound, we implement an empirical correction factor of 2. This upward shift forms a reliable envelope that safely bounds the worst-case line-pulling dynamics demonstrated across all simulated parameters.

Consequently, the definitive equation used to assess the lineshape asymmetry uncertainty throughout this work is:

$$\sigma_{\text{asym}} = 2 \times \delta\nu_{\text{span}} \times \frac{S_{\text{pp,asym}}}{S_{\text{pp,signal}}} \tag{19}$$

Finally, evaluating the entire experimental dataset using any of the discussed error-bounding models ultimately yields final averaged combination results that agree well within their 1σ statistical uncertainties. This confirms that the final physics extraction is highly robust against the specific choice of systematic error derivation, ensuring the absolute stability of our reported central frequency values.

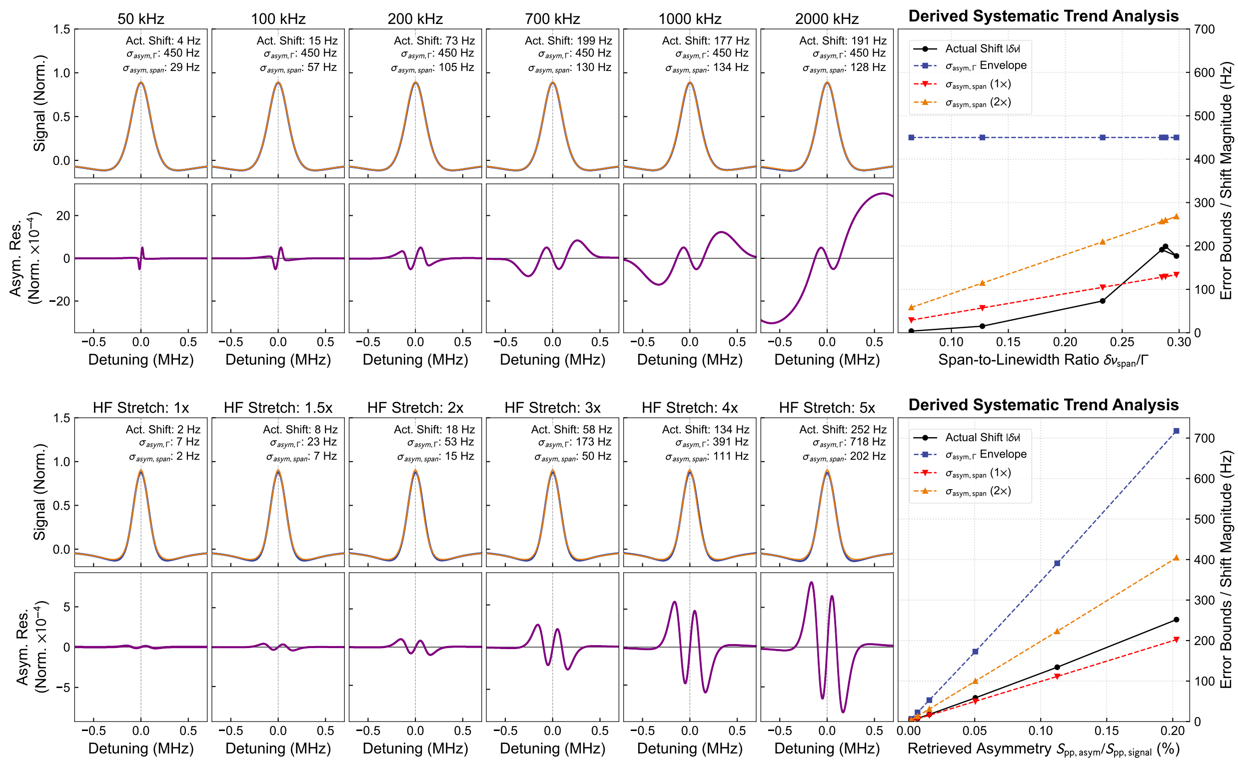

FIG. 2. Numerical simulations of line-pulling systematic effects under two independent perturbation mechanisms. The top rows illustrate an instrumental background perturbation (dispersive injection track) where a synthetic windowed dispersive artifact is introduced at varying background spans ($\delta\nu_{\mathrm{bg}}$) and iteratively normalized to a fixed 0.1% peak-to-peak amplitude. The bottom rows illustrate a physical structural perturbation (hyperfine multiplet track) where the splitting constants of the 22 composite methanol transitions are expanded via a stretch factor from 1× to 5×. In the individual profile panels, the upper plots show the normalized composite signal alongside the symmetric Lorentzian fit, and the lower plots showcase the isolated, zero-centered asymmetric residuals. The summary trend analysis charts on the right compare the actual fitted center frequency shift (black solid line) against the bounds predicted by the global linewidth model $\sigma_{\mathrm{asym},\Gamma}$ (blue dashed line), the unscaled localized model $\sigma_{\mathrm{asym,span}}$ (1× local span, red dashed line), and the empirically scaled model (2× local span, orange dashed line) as a function of the span-to-linewidth ratio (top right) and the retrieved peak-to-peak asymmetry amplitude (bottom right).

IV. LONG-TERM REPRODUCIBILITY OF THE MEASUREMENT SETUP

To evaluate the long-term stability of the spectrometer and constrain potential systematic frequency drifts over extended timescales, we performed a continuous, back-to-back measurement run consisting of 60 scans over an 8-hour period on the $\Delta_{3,1}$ transition. The time-series analysis of the extracted line centers ($\nu_{\rm fit}$) is displayed in Fig. 3.

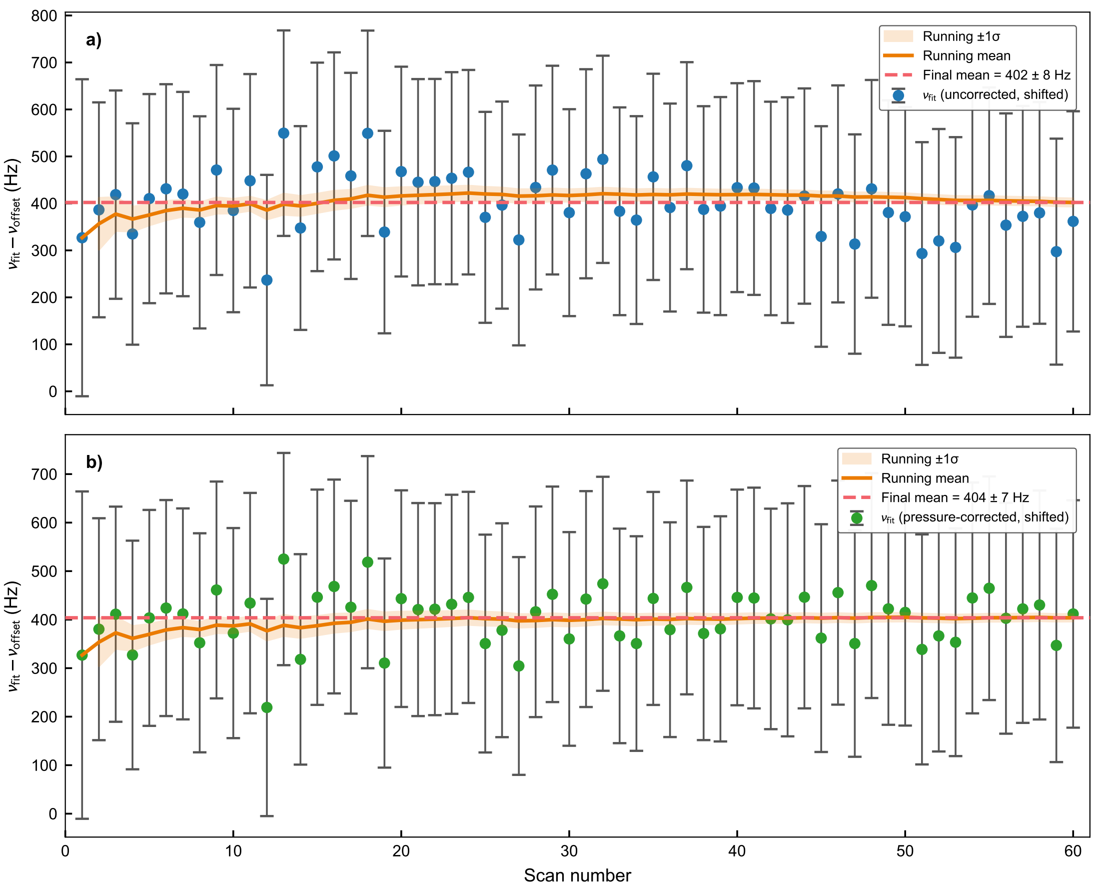

FIG. 3. Statistical reproducibility of the $\Delta_{3,1}$ transition frequency ($\nu_{\rm fit}$) at 7191.0673 cm^{-1} recorded continuously over an 8-hour period. Data points represent individual scans recorded at 0.0625 Pa nominal pressure, 1 W intracavity power, and 150 kHz dither amplitude. The vertical axis displays $\nu_{\rm fit}$ relative to an offset $\nu_{\rm offset} = 215\,582\,774\,000$ kHz. Error bars indicate the 1σ single-scan fit uncertainty ($\sigma_{\rm fit}$), while the shaded bands show the running mean and its standard error. Panel (a) shows the raw line centers, where a minor, slow frequency drift is present due to passive pressure variations. Panel (b) displays the data after applying a line-by-line correction using the pressure-shift coefficient ($c_p = 13.2$ kHz/Pa), isolating the flat instrumental baseline.

The raw line centers in Fig. 3(a) show a highly stable baseline over several hours, free from abrupt jumps or systematic instrumental signatures. The only visible drift is a slow frequency wander that correlates with small, passive variations in the sample pressure. Because the gas handling system relies on the passive stability of a manually adjusted leak valve, minor variations of the pressure equilibrium occur naturally over long periods.

Since the pressure is logged during data acquisition, this small effect can be compensated for using the linear pressure-shift coefficient ($c_p = 13.2$ kHz/Pa) determined from the global regression model. The resulting pressure-corrected dataset is shown in Fig. 3(b). The corrected data forms a flat baseline centered at 404 ± 7 Hz relative to the plotting offset. The absence of any residual drift confirms that long-term variations from instrumental systematics, such as residual amplitude modulation (RAM), are negligible at our precision level.

The single-scan fit uncertainties, represented by the error bars on the individual points, are systematically overestimating the actual point-to-point scatter of the apparatus and are dominated by the symmetric residuals (as discussed in the main text). A statistical analysis of the observed scatter shows that the short-term reproducibility of the spectrometer is superior to the uncertainty limits returned by individual profile fits. Based on the observed point-to-point spread, the pressure-corrected ensemble converges to a robust statistical uncertainty floor of ± 7 Hz. This exceptional reproducibility demonstrates the reliability of our spectrometer deep within the tens-of-Hz regime.

V. LINEWIDTH ANALYSIS AND SATURATION REGIME

To accurately evaluate potential systematic lineshape distortions and transit-time effects, it is necessary to quantify the individual physical mechanisms contributing to the observed transition linewidth. As demonstrated in Section I of this Supplementary Material, the structural lineshape broadening contribution arising purely from the underlying hyperfine multiplet asymmetry is entirely negligible, amounting to merely ~ 1 kHz for our typical parent molecular widths. At the typical circulating powers of 1 to 2 W and the optimal dither amplitude of 150 kHz, the fitted $1f$-dispersive Lorentzian FWHM is consistently observed to be $\gamma \approx 450$ kHz. To isolate the pure power-broadened linewidth, we analyze the measurements for the $\Delta_{1,1}$ transition at 1 W, the minimum power level used in our experiment. At this power, the smallest zero-pressure extrapolated linewidth is measured to be 327 kHz (at 150 kHz dither).

Based on the data of the dither study (see Fig. 7 in main text), we deduce the added broadening from modulation to be ≈ 38 kHz. Subtracting this contribution yields a minimum extrapolated linewidth of 289 kHz, free from both collisional and modulation broadening. This is in excellent agreement with the simulated modulation spectrum presented in Section I of this Supplementary Material, where a matching 38 kHz dither-induced increase in the linewidth was determined. The observed line width for varying dither amplitudes are plotted in Fig. 4.

For a Gaussian beam with a waist radius of $w_0 = 0.72$ mm, the standard transit-time broadening limit for a thermal gas at our operating temperature ($T = 243$ K) is given by $\Gamma_{\text{transit}} \approx u/(\pi w_0)$ [2]. Here, $u = \sqrt{2k_BT/m} \approx 355$ m/s is the most probable 2D transverse speed for the methanol molecule ($m \approx 5.32 \times 10^{-26}$ kg). This yields a theoretical transit-time limit of $\gamma_0 \approx 157$ kHz.

The substantial discrepancy between this theoretical limit (157 kHz) and our isolated 289 kHz FWHM indicates that the transition is heavily dominated by power broadening. This ratio allows for a direct empirical deduction of the saturation parameter, S_0, at the center of the beam. In saturation spectroscopy, the power-broadened FWHM of the homogeneous Lamb dip relates to the unperturbed transit-time width via $\gamma = \gamma_0\sqrt{1+S_0}$ [3]. Inverting this relation yields:

$$S_0 = \left(\frac{\gamma}{\gamma_0}\right)^2 - 1 \tag{20}$$

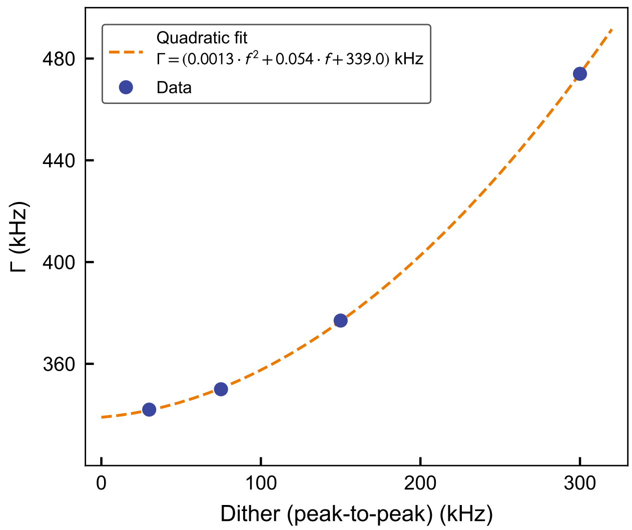

FIG. 4. Observed linewidths of the $\Delta_{1,1}$ transition (at 1 W intracavity circulating power) for various settings of the dither amplitude.

Using our isolated minimum width of $\gamma = 289$ kHz, we derive an empirical saturation parameter of $S_0 \approx 2.4$ at the lowest utilized optical power.

This analysis unequivocally demonstrates that the experiment operates well into the saturated regime ($S_0 > 1$) across all measurements. Because power broadening is a homogeneous mechanism, this saturation forces the fundamental molecular resonance to remain strongly Lorentzian.

[1] B. Lankhaar, G. C. Groenenboom, and A. van der Avoird, Hyperfine interactions and internal rotation in methanol, J. Chem. Phys. **145**, 244301 (2016).

[2] C. J. Bordé, J. L. Hall, C. V. Kunasz, and D. G. Hummer, Saturated absorption line shape: Calculation of the transit-time broadening by a perturbation approach, Phys. Rev. A **14**, 236 (1976).

[3] W. Demtröder, *Laser Spectroscopy, 4th Edition* (Springer, 2008).